INL/JOU-22-67897-Revision-1

Lithium inventory tracking as a non-destructive battery evaluation and monitoring method

March 2024

Boryann Liaw, Meng Li, Yulun Zhang, Hui Zhou, Fengxia Xin, M. Stanley Whittingham

INL/JOU-22-67897-Revision-1

Lithium inventory tracking as a non-destructive battery evaluation and monitoring method

Boryann Liaw, Meng Li, Yulun Zhang, Hui Zhou, Fengxia Xin, M. Stanley Whittingham

March 2024

Idaho National Laboratory
Idaho Falls, Idaho 83415

http://www.inl.gov

Prepared for the
U.S. Department of Energy
Under DOE Idaho Operations Office
Contract DE-AC07-05ID14517

Lithium Inventory Tracking as a Nondestructive Battery Evaluation and Monitoring Method

Meng Li[1], Yulun Zhang[1], Hui Zhou[2], Fengxia Xin[2], M. Stanley Whittingham[2], and Boryann Liaw[1,z]

[1] Energy Storage and Electric Transportation, Idaho National Laboratory, Idaho Falls, ID 83415, USA

[2] The NorthEast Center for Chemical Energy Storage, Binghamton University (SUNY), Binghamton, NY 13902-6000, USA

[z] Corresponding Author E-mail Address [boryann.liaw@gmail.com]

Abstract

Tracking active lithium (Li) inventory in an electrode shows the true state of a Li battery, akin to a fuel gauge for an engine. However, nondestructive Li inventory tracking is currently unavailable. Here we used the theoretical capacity of a transition metal oxide to convert capacity into a Li inventory analysis. The Li inventory in electrodes was tracked reliably to show how battery formulations and test methods affect performance. Contrary to capacity, Li inventory tracking reveals stoichiometric variations near the electrode-electrolyte interface. Verifiable results rationalized the differences in measurements, clarifying and reducing interferences from cell formulations and experimental manipulations. By tracing four variables from the formation to end-of-life, we characterize electrode and cell performance with a thermodynamic framework. Accurate rationalization of subtle differences in Li inventory utilization promises precise battery engineering, evaluation, failure analysis, and risk mitigation. The method could be applicable from cell design optimization, fabrication, to battery management, improving battery performance and reliability.

Main Text

Lithium (Li) inventory tracking to trace Li inventory in cathode active material (CAM) and its utilization in a rechargeable Li battery from formation to end-of-life (EOL) is highly desired because the Li inventory reflects the true state of a battery. However, no accessible method can monitor active Li inventory in a battery. Measuring accumulative charge is the present way to assess the capacity that may be available to sustain cell operation, and Coulombic efficiency (CE) marks the charge retention efficiency of each charge-discharge cycle. Side reactions and self-discharge could invalidate or skew accurate estimation of usable capacity in a battery during operation or over its lifetime.[1-14] Capacity analyses often result in finite extrapolation of measured data and questionable inference to performance characteristics in practical uses. Tracking active Li inventory may provide truthful information for the intended use of a battery. High nickel (Ni)-content layered transition metal oxides like $Li_xNi_{0.8}Mn_{0.1}Co_{0.1}O_2$ (NMC 811) are attractive for high-energy rechargeable Li battery applications.[15] To evaluate CAM's performance and its potential for intended applications, measuring and analyzing capacity is a typical method practiced.[1-14] The method measures the voltage versus capacity relationship by a test protocol. By using a matrix of cell formulation and design, the choice is empirically made by performance metrics from testing. This empirical method lacks a theoretical basis to verify and validate the results reliably. Thus, this empirical approach needs intensive resources in cell design and performance optimization, while the result may not be as satisfactory as expected. A theoretical principle-backed approach to pursue such an engineering optimization and validate results in a rationalized manner can save cost, labor, energy, and time, thus highly desirable.

Here, a matrix of 12 Li–NMC 811 cells made of various cell formulations and configurations (**Table 1**) and subjected to tests under different protocols and conditions is chosen as a case study to illustrate the needs and merits of Li inventory tracking. Such an asymmetric set of test data is traditionally difficult to analyze and rationalize for a clear understanding of the cause-and-consequence relationship. The variants in this matrix include, e.g., pristine Targray (T) and EcoPro (E) NMC 811 different in morphologies and grain size distributions, cathodes made by different fabrication processes, electrolytes of different formulations, and cell types in coin (C) and pouch (P) formats. Furthermore, cells of the same makeup were evaluated under different protocols and conditions in formation and cycle aging processes. In this paper, we shall focus on proving the concept and principle of Li inventory tracking using this matrix. We show that rationalized comparisons and interpretations of the experimental results, including first cycle capacity loss (FCCL),[16-24] can be achieved and verified. A thermodynamic framework using an equilibrium potential (V_{eq}) versus Li inventory (i.e., x in the NMC 811 stoichiometry) or "V_{eq} vs. x" relationship was applied to compare results in the matrix. Lithium inventory variation in charge or discharge process was elucidated and cathode utilization quantified in the respective segment. A rationalized approach was demonstrated as a cross-platform tool capable of comparing results from cells of dissimilar formulations or of the same formulation but in different test conditions. The approach revealed CAM utilization and cell performance in depth that the capacity analyses could not offer.

Table 1 | **The matrix of exemplified cells in this work**. LP30 is Gotion electrolyte comprised 1.0 M lithium hexafluorophosphate ($LiPF_6$) dissolved in ethylene carbonate (EC)-dimethyl carbonate (DMC) solution (1:1 in weight). M47 is a localized high-concentration electrolyte (LHCE) with lithium bis(fluorosulfonyl)imide (LiFSI), 1,2-Dimethoxyethane (DME), 1,1,2,2-Tetrafluoroethyl-2,2,3,3-tetrafluoropropyl ether (TTE) at a molar ratio of 1:1.2:3. Gen2 electrolyte comprised 1.2 M $LiPF_6$ in a 3:7 (w/w) mixture of EC and ethyl methyl carbonate (EMC) with 2 wt% vinylene carbonates (VC).

Cell ID	Cathode	Cell Configuration	Cell Type	Test Protocol
E-C	EcoPro NMC 811	Li | LP30 | E-NMC 811	Coin	Formation cycle
T-C	Targray NMC 811	Li | M47 | T-NMC 811		
T-P		Li | LP30 | T-NMC 811	Pouch	
GITT_4.2	EcoPro NMC 811	Li | Gen2 | E-NMC 811	Coin	GITT (Formation cycle)
GITT_4.4				
GITT_4.6				
Form_4.2				Formation cycle
Form_4.4				
Form_4.6				
CA_4.2				Cycle aging at C/3
CA_4.4				
CA_4.6				

Comparing Cells of Different Formulations or Test Conditions

The first nine cells in **Table 1** all went through a formation cycle (while the last three through cycle aging) but with two different formation protocols. The asymmetric metrics in formulation among the nine make the results hard to analyze and reach a rationalized conclusion today. **Fig. 1a** shows the voltage (V) vs. specific capacity (Q) profiles of the nine, all starting with pristine NMC 811. Among them, E-C, T-C, and T-P are asymmetric in formulations and cell types/sizes but subjected to the same protocol. This scenario presents a challenge in cell design, scale-up, and optimization, where a rationalized conclusion might be hard to attain. In contrast, the next six (i.e., three from GITT_4.2 to GITT_4.6 and from FORM_4.2 to FORM_4.6, respectively) are of the same formulation but subjected to two formation protocols. This scenario spells out a challenge in deciphering root causes and their impacts on cell performance from variations in test protocols and conditions. Both scenarios are common hurdles we face today in empirical approaches, where no theoretical framework can guide battery design by principles and support precise engineering by a rationalized method to verify results. Similarly, to assess performance of a cell design, CA_4.2, 4.4, and 4.6 went through cycle aging in different V_{max} charge cutoff conditions and showed noticeable disparities in charge retention and degradation. This scenario calls for a definitive method to explain these results so the cell design can be validated. Such a

method remains lacking to define the accuracy for verification and validation, but in this work, we showed that it is achievable.

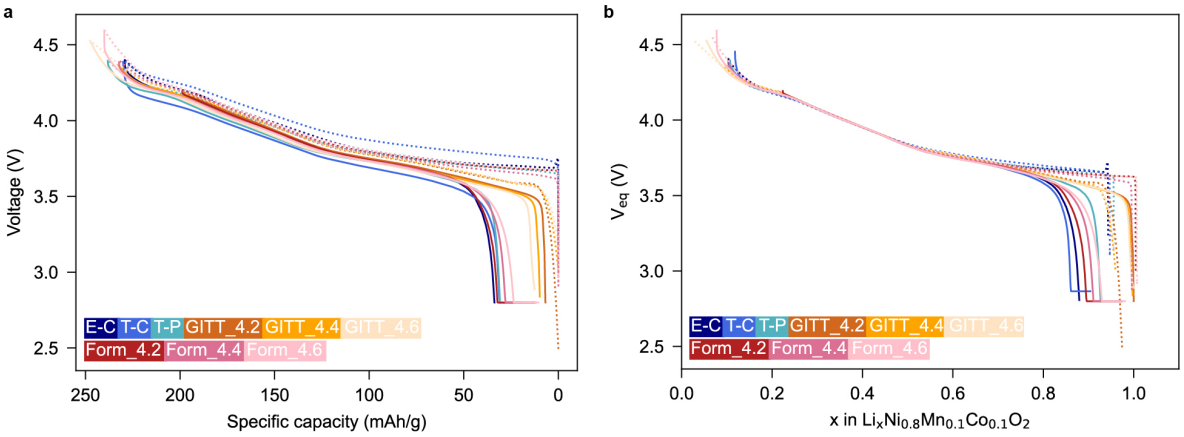

Fig. 1 | Test results and Li inventory tracking of nine cells in the formation cycle. a, Results of the nine cells presented in voltage vs. specific capacity curves in the formation cycle. **b**, The results presented in a V_{eq} vs. *x* relationship.

In **Fig. 1b**, our analytic approach transforms the results in **Fig. 1a** into a V_{eq} vs. *x* relationship. **Supplementary Fig. 1** and the related explanation in **Supplementary Discussion** depict the data reduction workflow in Supplementary Information. Here, the actual Li inventory or Li content in NMC 811 stoichiometry (*x*) show definitive variations among the nine cells while their formulations and test conditions were different. The distinctions become identifiable for detailed examinations. The data transformation from **Fig. 1a** to **Fig. 1b** properly removes the polarization potential from the measured voltage to reveal the V_{eq} of the cathode against Li metal. The correspondence of V_{eq} and *x* is further explained as follows:

Equilibrium Potential versus Li Inventory Relationship

Lithium inventory tracking hinges on a reliable equilibrium potential (V_{eq}) vs. Li inventory relationship. This relationship is governed by Gibbs free energy of formation of NMC 811 as a function of the Li content (*x*) in the stoichiometry.[25,26] The relationship is typically determined by the galvanostatic intermittent titration technique (GITT) where the Li content is supposed to alter stepwise with a certain incremental specific capacity ΔQ and a V_{eq} is determined over a sufficiently long rest. As an example, **Fig. 2a** shows the result of a GITT formation cycle obtained from cell GITT_4.4 which is made of pristine EcoPro NMC 811. The formation was conducted between V_{min} = 2.8 V and V_{max} = 4.4 V at C/20 rate. **Fig. 2b** exhibits the V_{eq} vs. specific capacity (Q) relationship in the formation. In GITT, "1:1 correspondence" between ΔQ and Li content change (Δ*x*) is used to give the V_{eq} vs. *x* relationship as presumed. If so, we should expect V_{eq}'s from the charge and discharge segments should fall on each other, since the same ΔQ was used in the two segments. However, the results in **Fig. 2b** show disagreement. The disagreement between the charge and discharge segments showed larger magnitudes than errors in the resolution of the data acquisition system. Thus, the differences cannot be explained by experimental or systematic errors. Furthermore, the differences accumulated through cycling, so they are not simply noise or random errors.

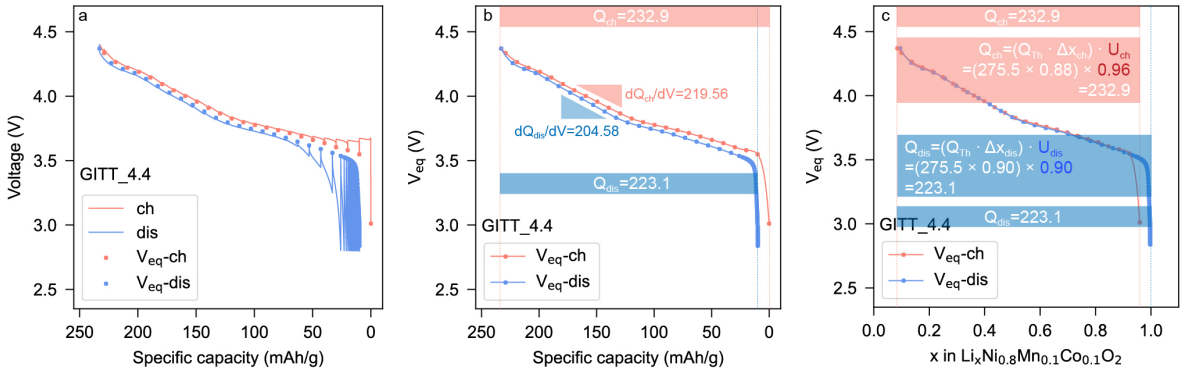

Fig. 2 | The charge-discharge profiles of a GITT formation cycle. **a**, The voltage profiles of GITT_4.4 in a GITT experiment conducted at C/20 with a constant ΔQ increment. **b**, The V_{eq} vs. Q profiles. **c**, Transformed V_{eq} vs. *x* curves if theoretical capacity Q_{Th} of NMC 811 and utilization efficiency **U** were considered in each segment.

To resolve this disagreement between the charge and discharge segments in GITT, we shall employ the theoretical capacity of NMC 811 to understand and verify the results in **Fig. 2b** in a rationalized approach. Based on the NMC 811 chemical formula, the theoretical capacity of NMC 811 Q_{Th} is 275.5 mAh g^{-1}, representing the capacity corresponds to varying one Li in the NMC 811 stoichiometry, or $dQ_{Th}/dx|_{(\Delta x=1.0)}$ = 275.5 mAh g^{-1}. Thus, were the electrode material fully utilized in a charge or discharge process, every fraction of one Li removes from or insert into NMC 811 should result in a corresponding change in specific capacity. From the V_{eq} vs. Q profile, an incremental capacity change (dQ/dV) could be derived from the region between 4.10 V and 3.90 V, where the capacity retention is considered highly reversible and most sensitive. By examining the data in **Fig. 2b** we found that dQ_{ch}/dV = 219.56 mAh g^{-1} and dQ_{dis}/dV = 204.58 mAh g^{-1} in the charge and discharge segment, respectively. The difference between the two is so large that it cannot be just experimental errors. Applying $dQ_{Th}/dx|_{(\Delta x=1.0)}$, we transformed the V_{eq} vs. Q profiles into V_{eq} vs. *x* curves for the charge and discharge segment respectively (**Fig. 2c**). Here, the two V_{eq} vs. *x* curves aligned closely in good agreement. Such agreement suggests that the GITT data indeed reflects the principle as it was supposed to, but getting the correct correspondence needs careful verification.

Learning from this example, we realized that the Li stoichiometric variation Δ*x* and capacity change ΔQ do not follow the "1:1" ratio as presumed. Instead, a CAM utilization coefficient **U** is required to depict such correspondence by:

$$\mathbf{U} = Q / (Q_{Th} \times \Delta x) \quad (1)$$

The establishment of this relationship is profoundly useful. Now, we can carefully analyze each charge and discharge segment with accuracy to rationalize results and implications from cell evaluation. This procedure (as outlined in **Supplementary Fig. 1** and further explained in **Supplementary Discussion**) was applied to the remaining eight cells, as shown in **Fig. 1b**. The results derived from each of the V_{eq} vs. *x* curves are summarized in **Table 2**. The utilization efficiency of cathode in each charge or discharge segment can now be calculated.

Table 2 | Summary of the analyses on formation cycle of the first nine cells.

Cell ID	Q_{ch} (mAh g^{-1})	Q_{dis} (mAh g^{-1})	CE (%)	dQ_{ch}/dV (mAh g^{-1} V^{-1})	dQ_{dis}/dV (mAh g^{-1} V^{-1})	U_{ch}	U_{dis}	Transverse x_{ch}	Transverse x_{dis}	Δx_{ch}	Δx_{dis}
E-C	229.20	195.42	85.26	228.61	204.49	1.00	0.90	0.94 → 0.10	0.10 → 0.88	0.84	0.78
T-C	230.08	198.88	86.44	227.64	221.62	1.00	0.97	0.95 → 0.11	0.12 → 0.86	0.84	0.74
T-C (w/ CV)	230.08	210.51	91.49	227.64	221.62	1.00	0.97	0.95 → 0.11	0.12 → 0.90	0.84	0.78
T-P	238.19	207.34	87.05	226.75	206.32	0.99	0.91	0.96 → 0.10	0.11 → 0.93	0.86	0.82
GITT_4.2	199.16	192.31	96.56	213.41	201.97	0.94	0.89	0.97 → 0.21	0.21 → 1.00	0.76	0.79
GITT_4.4	232.91	223.09	95.78	219.56	204.58	0.96	0.90	0.96 → 0.09	0.10 → 1.00	0.87	0.90
GITT_4.6	247.63	235.11	94.94	217.91	205.29	0.96	0.90	0.96 → 0.03	0.06 → 1.00	0.93	0.94
Form_4.2	198.75	166.57	83.81	211.81	202.09	0.93	0.89	1.00 → 0.23	0.23 → 0.90	0.77	0.67
Form_4.2 (w/ CV)	198.75	185.85	93.51	211.81	202.09	0.93	0.89	1.00 → 0.23	0.23 → 0.97	0.77	0.74
Form_4.4	232.24	204.17	87.91	211.22	205.12	0.93	0.90	1.00 → 0.10	0.10 → 0.91	0.90	0.81
Form_4.4 (w/ CV)	232.24	220.14	94.79	211.22	205.12	0.93	0.90	1.00 → 0.10	0.10 → 0.97	0.90	0.87
Form_4.6	240.07	216.46	90.16	210.08	206.74	0.92	0.91	1.00 → 0.07	0.08 → 0.93	0.93	0.85
Form_4.6 (w/ CV)	240.07	229.48	95.59	210.08	206.74	0.92	0.91	1.00 → 0.07	0.08 → 0.98	0.93	0.90

A distinctive aspect between the results in **Fig. 2b** and **Fig. 2c** is the transverse stoichiometric change $\Delta x_{dis} = 0.90$, which is larger than $\Delta x_{ch} = 0.87$, whereas $Q_{dis} = 223.09$ mAh g^{-1} is smaller than $Q_{ch} = 232.91$ mAh g^{-1} due to a noticeable disparity between $\mathbf{U_{dis}} = 0.90$ and $\mathbf{U_{ch}} = 0.96$. Here, the concept of electrode utilization coefficient **U** needs further explanation to clarify its origin. In **Supplementary Fig. 2**, we provide a schematic to depict the concept, and additional comments are in **Supplementary Discussion**. In battery testing, the tester executes the test protocol at the current leads that connect to current collectors or tabs on the electrode to permit the voltage and current be measured and manipulated. However, to utterly understand cell behavior, the electrochemical potential is more relevant. Of the cathode, the potential is determined near the cathode-electrolyte interface.[27] As the cathode electrochemical potential is governed by the Li activity at the cathode-electrolyte interface, whereas the testing or power control device senses and manipulates a voltage difference between the two current leads, there is a Li concentration gradient between the two that is governed by Li diffusion or ion transport in the cathode affected by the current flow driven by such a potential difference. The utilization coefficient **U** reconciles the capacity Q (that is dispersed in the electrode) with the Li inventory change ($Q_{Th} \times \Delta x$) monitored near the cathode-electrolyte interface.

It is clear now that without considering variables **U**, transverse x (which marks the terminal stoichiometry at the beginning and the end of a charge or discharge segment), and Δx (which depicts the change in stoichiometry in the respective segment), extracting data and interpreting experimental results by capacity analysis could be abstract in assessing the impacts of the test protocol and condition on cathode performance and degradation. The method of Li inventory tracking fills that gap. Considering V and Q are both floating (undefined) variables to the actual cathode potential depicted by Li activity and reactivity near the cathode-electrolyte interface, capacity analysis is extrapolating information over the thickness of cathode (accompanied with ill-defined topologies of electrical contact and electrolyte flow field resulting from variations in localized loading/packing density and porosity distributions). Thus, capacity analysis cannot assess the severity of the impacts accurately. For instance, the result in **Fig. 2b** indicated that the cathode was not fully discharged as sensed by the tester in the voltage and capacity control. Yet, the analysis in **Fig. 2c** indicated that the stoichiometry of the cathode in the region close to the separator was fully discharged—a stark contrast to the results in **Fig. 2b**. By Li inventory tracking, accurate assessment should prevent unintentional overcharging or over-discharging in the cell. This implication is evident in many microscopic or spectroscopic studies about the presence of spinel-like or rock salt structures and microdomains near the surface of the cathode or cathode secondary particles in cycle aging.[28,29] Our analysis provides a plausible explanation why such phase transformations to spinel-like and rock salt microdomains would happen in the surface region. Another intriguing aspect is hysteresis,[30-33] a phenomenon that is observed but its origin debated. The data in **Fig. 2b** could be considered as a hysteresis, if the correspondence with Li content was not carefully investigated and verified as shown in **Fig. 2c**.

With the concept of Li inventory tracking and cathode utilization efficiency explained above, a thermodynamic framework and a reliable, consistent basis for analyses are now accessible. The cell matrix in **Table 1** and results in **Table 2** allow us to pursue a careful examination of the data and performance characteristics among the first nine cells as follows:

Same Protocol but Different Cell Formulations

Supplementary Fig. 3 shows the comparisons among E-C, T-C, and T-P cells. The results in typical V vs. Q profiles as shown in **Supplementary Fig. 3a** suggest the protocol produced comparable results with three cells despite their makeups and cell types. This conclusion by empirical capacity comparison gives no clear answer as to why we could not tell any definitive differences. For instance, since T-C and T-P cells used the same electrode materials and went through the same formation protocol, does the cell type matter? LP30 electrolyte was used in T-P, whereas a localized high-concentration electrolyte (LHCE) M47 was in T-C. Is the electrolyte relevant? Likewise, should differences in particle size distribution and morphology between EcoPro and Targray particles make any distinction in formation?

Here, the Li inventory analysis in **Supplementary Fig. 3b** shows that certain differences in the properties of the pristine cathodes, cell formulations, and performance characteristics could be identified and verified. For instance, the pristine Li content in three cathodes varied. Compared to the unified V_{eq} vs. x curve determined by GITT in **Fig. 2b**, these cathodes might have been interfered by various degrees of surface contamination,[34] causing disparities in initial x_{ch} and resulting Δx_{ch} in the charge segments. However, such contamination did not affect $\mathbf{U}_{ch}$. All three showed high $\mathbf{U}_{ch} \approx 1.00$, and Δx_{ch} (E-C) = 0.84 < Δx_{ch} (T-C) = 0.87 ≈ Δx_{ch} (T-P) = 0.86, coinciding with the trend in capacity: Q_{ch} (E-C) = 229.2 < Q_{ch} (T-C) = 238.3 ≈ Q_{ch} (T-P) = 238.2 mAh g^{-1}. In the discharge segment, the trend: Q_{dis} (E-C) = 195.4 < Q_{dis} (T-C) = 207.8 ≈ Q_{dis} (T-P) = 207.3 mAh g^{-1} showed that CE (E-C) = 85.3% < CE (T-C) = 87.2% ≈ CE (T-P) = 87.1%. Similarity in the formation results between T-C and T-P seem to mask the anticipated effects from cell type and electrolyte. Although the difference in cell type could be addressed by area specific impedance (ASI) and related to solid-electrolyte interphase formation as an electrolyte effect, its impact on capacity remains unclear. An impact from electrolyte was suggested by $\mathbf{U}_{dis}$ (T-C) ≈ 0.97 (for LHCE), which is better than $\mathbf{U}_{dis}$ (T-P) = 0.91 ≈ $\mathbf{U}_{dis}$ (E-C) = 0.90 (where cells used LP30 or Gen2 electrolytes showed similar $\mathbf{U}_{dis}$ around 0.89 ~ 0.91). This result suggests that LHCE indeed promoted interfacial kinetics and reduced Li concentration gradient-induced surface effect. But the sluggish Li transport in the bulk[16-23] still constrained depth-of-discharge (DOD) in T-C as shown by Δx_{dis} (T-C) = 0.74 before the constant voltage (CV) step. With the CV step, Δx_{dis} (T-C) = 0.78 is just as good as Δx_{dis} (E-C) = 0.78 and still less than Δx_{dis} (T-P) = 0.82. This observation implies that a better electrolyte could improve cathode surface stability but not necessarily capacity. A higher Δx_{dis} in T-P could be due to cell type and lower ASI. In this example, we should focus on the ability in analyzing data from an asymmetric matrix that is difficult to achieve usually. From similarities and distinctions via Li inventory tracking, we showed how performance metrics were affected by attributes that are difficult to distinguish traditionally, e.g., Q_{FCCL} (E-C) = 33.78, Q_{FCCL} (T-C) = 30.53, and Q_{FCCL} (T-P) = 30.85 mAh g^{-1} is about the same even though the respective Δx_{dis} and $\mathbf{U}_{dis}$ are different by electrolyte and cell type. We dare not to suggest that these results are always true but to emphasize the benefit of Li inventory tracking that can provide truthful analytics. To decipher how cell formulations affect performance, we believe that sufficient dataset and comparisons will be needed to clarify what really matters. The most critical aspect is that the insight is verifiable by this Li inventory tracking now.

Same Cell Formulation but Different Protocols

Supplementary Fig. 4 shows the comparison among the three GITT cells with different V_{max} cutoffs in the formation cycle. A trend depicts that attainable capacity increased with higher V_{max} towards EOC and BOD but decreased (i.e., to a less extent in DOD) towards EOD, as shown in **Supplementary Fig. 4a**. The Q_{FCCL} follows the trend of 6.85 mAh g^{-1} in GITT_4.2 < 9.82 mAh g^{-1} in GITT_4.4 < 12.52 mAh g^{-1} in GITT_4.6 with a constant increment of loss about 3 mAh g^{-1} per 0.2 V of increase in V_{max}. This incremental loss with V_{max} suggests the cells could only reach a lower DOD with increasing V_{max}. It is hard to decipher from the capacity what caused the disparities among the three cells due to the different V_{max} cutoffs in the GITT protocols.

Supplementary Fig. 4b reveals that the stoichiometries at the BOC and EOD are almost identical among the three cells. The excellent alignment among the three V_{eq} vs. x profiles demonstrates a unified V_{eq} vs. x curve is attained and verified, and this unified curve can be used as the basis for cross-platform analyses. Even with different V_{max} cutoffs, the GITT protocols yielded similar NMC 811 utilization efficiency in all three. The V_{max} cutoffs are the causes that led to the disparities in the transverse x and Δx as anticipated (see **Table 2**), i.e., the terminal x_{ch}'s at EOC are 0.21, 0.09, and 0.03, and Δx_{ch} = 0.76, 0.87, and 0.93, respectively for the three cells in the charge segment. In the discharge segment, all three reached x_{dis} = 1.00 at EOD with Δx_{dis} = 0.79, 0.90, and 0.94, respectively. The differences in Q_{FCCL} might be an accumulated result of the slight variations in **U** and Δx_{cycle}, which are difficult to discern since the magnitude of uncertainty is within the experimental errors. In other words, we could not conclude if the steady increasing Q_{FCCL} fade with V_{max} truly has a real underlying mechanism to explain such a trend except the slow Li transport. However, it is important to note that the 4.6 V cutoff could only reach a state settled near V_{eq} = 4.51 V at EOC and BOD (**Supplementary Fig. 4b**). There was a displacement in Li content between the two terminal states, suggesting a definitive Li inventory loss caused by, e.g., phase transition from layered to spinel-like/rock salt structures or formation of cathode electrolyte interphase (CEI), whereas GITT_4.2 and GITT_4.4 did not show such a result. The verification of the results in **Supplementary Fig. 4b** provides a reliable V_{eq} vs. x profile as a thermodynamic framework for the follow-on analyses in this work.

Supplementary Fig. 5 shows the results of FORM_4.2, 4.4, and 4.6 cells using a constant current (CC) C/10 rate charge and discharge cycle as a formation protocol with three different V_{max} cutoffs. The V_{eq} vs. Q profiles show a consistent trend of an increasing extent of DOD with a higher V_{max}, as shown in **Supplementary Fig. 5a**. This trend is opposite to the one with GITT formation. **Supplementary Fig. 5b** shows that this trend indeed persists in the Li inventory analysis, suggesting that the CC formation protocol created small but positive impacts from the increases in V_{max}, contrary to the GITT formation protocol. The different results between CC and GITT formation protocols may attribute to the equilibration in the rest period in the GITT formation that diminish the impact from the slow Li electrochemical diffusion in NMC 811. But GITT protocol still yield a higher Q_{dis} due to a larger Δx_{dis} in each case. The impacts from the higher V_{max} on $\mathbf{U_{dis}}$ are subtle, although $\mathbf{U_{dis}}$ = 0.89, 0.90, and 0.91 increases with 4.2 V, 4.4. V, and 4.6 V cutoff. There was a constant voltage step at 2.8 V after

EOD to recover the Li inventory, and the terminal point of this step reached an identical stoichiometry, verifying the small reduction in Q_{FCCL} = 12.90 (FORM_4.2), 12.10 (FORM_4.4), and 10.59 mAh g^{-1} (FORM_4.6) was the result of making up the differences in each Li inventory recovery in the discharge segment. The constant voltage step recovered most but not all the Li inventory but reached close to the stoichiometry at BOC. As suggested by Kang et al.,[17] the remaining Li inventory could be recovered if the V_{min} in the constant voltage step were further reduced to below 2.0 V. By now, we showed that, despite variations in cell formulation and test condition, tracking Li inventory can achieve rationalized and verifiable results consistently in cell formation.

The expectation of whether Li inventory tracking can be applied to cycle aging and achieve the same analytical merits should be demonstrated to show its viability in practical applications. Here, three E-C cells (CA_4.2, 4.4, and 4.6), representing a typical Li || NMC 811 chemistry, shall exemplify this aspect. These cells were subjected to cycle aging at C/3 with three V_{max} cutoffs, respectively, and the results were analyzed. **Fig. 3a** show capacity retention of the three. Cell CA_4.6 had the best retention, followed by CA_4.2. Cell CA_4.4 somehow exhibited surprisingly severe degradation than the other two after cycle 20. The erratic results are difficult to formulate a rationalized explanation by conventional capacity analyses. Here, we show that the Li inventory analyses can resolve such irrational results, demonstrating an unprecedented capability this technique can provide.

Cycle Aging Effects and Analyses

Fig. 3(b, c, d) show the sequential V vs. Q curves of these cells in cycle aging experiments, whereas **Fig. 3(e, f, g)** are the respective V_{eq} vs. *x* curves. The progression of the V vs. Q curves in cycle aging indicates that the three cells, even made of the same formulation, showed quite different responses under the cycle aging protocol with different V_{max} cutoffs. To rationalize why and how the V_{max} cutoffs affect the aging behavior of the cells in such a complex fashion, it is hard to achieve with typical capacity-based analytical approaches. There is an unspecified number of unclarified factors that could influence the severity of aging in each cell in a manner that is multifactorial, multimodal and multiscale, often dubbed as path dependence.[35,36] Such phenomena are commonly observed but also incomprehensible, because no tangible method is available to characterize such phenomena definitively. The Li inventory tracking method might be able to resolve such entanglements.

Taking in cell-to-cell variations to a proper perspective, even with complicated correlations and statistical analyses, a comprehensive approach is still unavailable to rationally identify and quantify all attributes to consequences and resolve the complex relationships among them. The variability comes in multitier and multidimensional aspects. For example, the variations could come from uncertainties in the material, electrode, and cell levels where control of processing parameters and conditions is critical to produce quality cells through quality control and quality assurance audits. These uncertainties are so difficult to identify that how to relate their relevant impacts on performance and to quantify the sensitivity in affecting cell quality auditing and subsequent degradation remain particularly challenging in failure mode and effect analysis. These uncertainties further percolate into cell formulation and fabrication. Even for a quality

product, the variations in duty cycle and schedule as reflected in test protocol could also lead to complicated contributions to variability. Thus, a case such as that in **Fig. 3**, even so simple in the design of experiment, exemplifies the need for a reliable analytic/diagnostic approach to clearly elucidate complicated cause-and-consequence relationship.

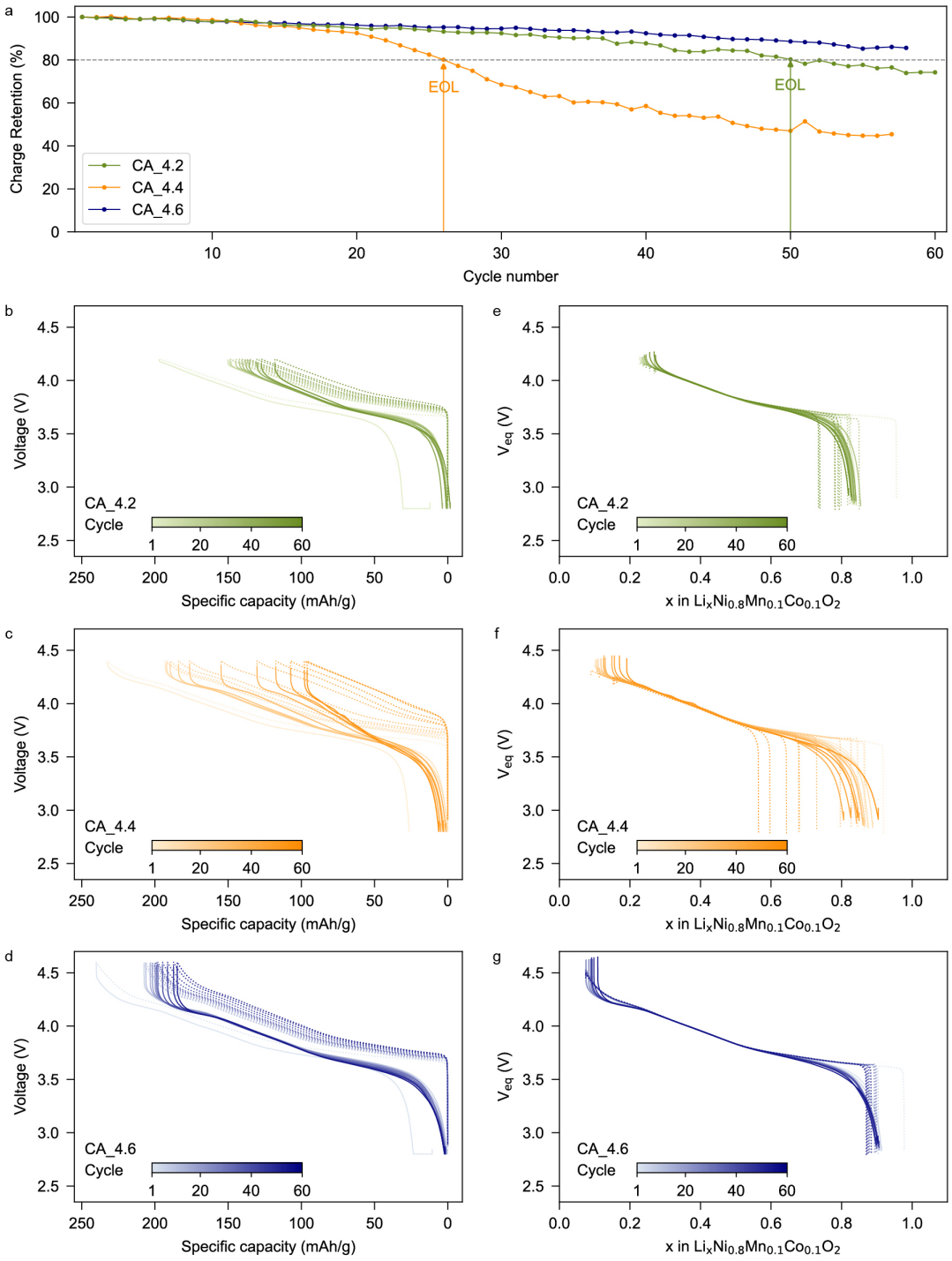

Fig. 3 | Test results of CA_4.2, 4.4, and 4.6 cells cycled at C/3 rate with three V_{max} cutoffs. **a**, Charge retention curves. **b**, Progression (over a certain interval of cycles) of the V_{eq} vs. x curves in cycle aging.

The reduction of **Fig. 3(e, f, g)** from **Fig. 3(b, c, d)** shows the benefit of Li inventory tracking. The data transformation removed the noisy polarization-related signals to provide a clear relationship in the progression of the cathode stoichiometry variation in the cycle aging. The ability to retain capacity in CA_4.6, followed by CA_4.2 and 4.4, was shown in **Fig. 3(e, f, g)** even though we do not understand the rationale. Additional diagnostic results are summarized in **Fig. 4**, showing how Li inventory tracking revealed critical aspects in a complicated cause-and-consequence relationship in cycle aging of these three cells.

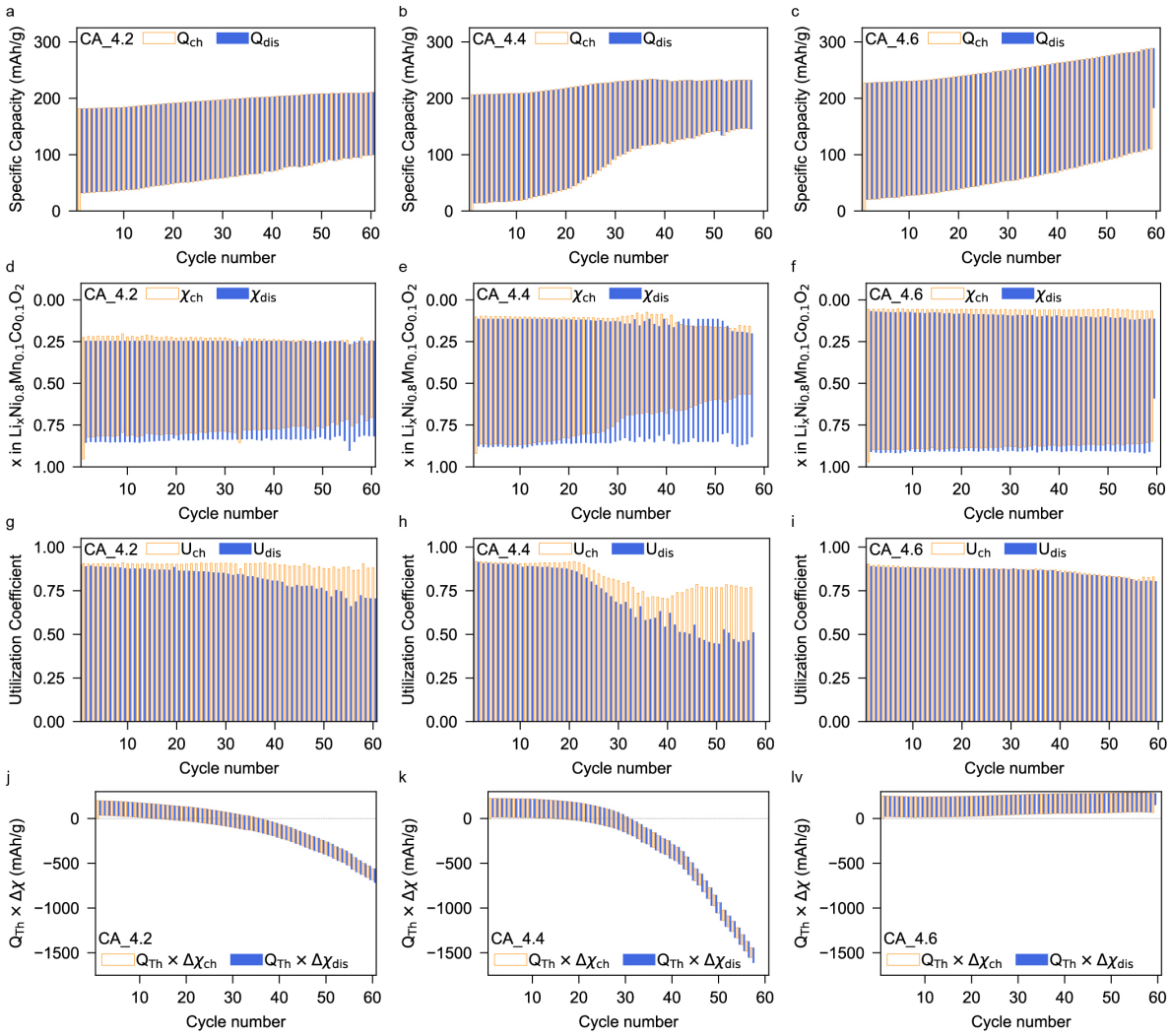

Fig. 4 | Tracing variations of critical variables in cycle aging performance in CA_4.2, 4.4, and 4.6 cells. **a-c**, Traces of capacity retention by specific capacity vs. cycle number. **d-f**, Traces of Li inventory changes in NMC 811 stoichiometry (x) as a function of cycle number. **g-i**, Traces of utilization coefficient **U** as a function of cycle number. **j-l**, Traces of ($Q_{Th} \times \Delta x$) as Li inventory by cycle number.

In **Fig. 4a-c**, the charge retention curves in **Fig. 3a** are shown by continuous traces of capacity variations in CA_4.2, 4.4, and 4.6, respectively, in cycle aging. Since Q_{dis} is usually less than Q_{ch}, the continuous trace shall depict an upward shift in capacity transactions along the charge and discharge endpoints over cycling. Thus, **Fig. 4a-c** exhibits how BOC/EOD and EOC/BOD drift with Q changes in cycle aging. **Fig. 4d-f** shows the corresponding stoichiometric drift in

NMC (by Li inventory tracking) with cycle aging, showing the transverse x_{ch} and x_{dis} endpoints and the respective Δx in each cell. **Fig. 4g-i** shows the accompanied utilization coefficient **U** in the charge and discharge segments in the aging process. **Fig. 4j-l** shows the traces of the Li inventory transactions in specific capacity ($Q_{Th} \times \Delta x$) that follows the transverse x_{ch} and x_{dis} endpoints and respective Δx during cycle aging in each cell. Here, it is important to point out that the traces of Q as shown in **Fig. 4a-c** were measured by the battery tester controller, yet the corresponding NMC stoichiometric traces were tracked in **Fig. 4d-f**, showing the variations of Li content near the cathode-separator interface in each cell cycle-by-cycle. The accompanied utilization coefficients **U**'s as shown in **Fig. 4g-i** reconciled the disparity between Q and ($Q_{Th} \times \Delta x$), whereas the cathode's Li inventory transactions were shown in **Fig. 4j-l**.

In **Fig. 4a-c**, CA_4.2 and CA_4.6 showed a continuous smooth drift in all endpoints in cycle aging, following the expectation of an imperfect charge retention, where Coulombic efficiency is typically less than unity. While CA_4.6 showed comparable drifts in both EOC/BOD and BOC/EOD trends, CA_4.2 showed more elevated drifts in BOC/EOD trendline, indicating a less efficient discharge in CA_4.2. The drifting in CA_4.4 was distinctly different from those two. As we inspect stoichiometric transversion in cathode (**Fig. 4d-f**), CA_4.6 showed a stable cycling behavior, where consistent EOC and EOD over cycles were observed, while BOD drifted downward and BOC upward gradually with cycling, consistent with gradual decrease of $\mathbf{U_{ch}}$ and $\mathbf{U_{dis}}$ (**Fig. 4i**) synergistically. The rate of decrease in **U** could be considered as the retardation of Li inventory retention over cycling. In **Fig. 3g**, a growing voltage hysteresis is also noted. If these observations were related, Li inventory tracking shown in **Fig. 4l** indicates that Li inventory loss was negligible, while capacity retention was suffered from Li diffusion kinetics and accumulative Li gradient buildup as hysteresis, eroding the utilization efficiency in CA_4.6.

The behavior might appear slightly different in CA_4.2. **Fig. 4d** shows that EOC gradually declined but BOD stayed about the same, suggesting the suffering of inefficient Li diffusion kinetics and accumulative Li gradient buildup, although $\mathbf{U_{ch}}$ remained about the same in the first 40 cycles (**Fig. 4g**). Meanwhile, EOD stayed the same, but BOC shifted upward and $\mathbf{U_{dis}}$ declined quite noticeably. These differences might appear subtle, but the pattern suggests that certain loss of Li inventory was incurring, and supply of Li inventory from the Li anode was necessary and gradually became constrained over cycling (**Fig. 4j**). Without Li inventory tracking as shown in **Fig. 4j**, the capacity tracking in **Fig. 4a** would not tell the difference and complexity in the mechanistic of degradation in CA_4.2 from CA_4.6. The inference made us suspect that the same Li inventory supply issue with Li anode could occur in CA_4.6 but it might be well delayed, starting after 40 cycles into the aging when the change of the rate in decade in both of **U**s appeared (**Fig. 4i**).

These examinations help the analysis of CA_4.4 degradation mechanistic, which appeared more complicated than the other two. By inspecting the traces in **Fig. 4b** and **k**, we thought of Li inventory could trace in three stages: (1) a regime where Li inventory predominantly lived on Li from pristine NMC (< 20 cycles in CA_4.4), (2) where Li inventory transitions from Li in pristine NMC to Li anode (cycle 21–33 in CA_4.4), and (3) where Li inventory is likely all from Li anode (> 34 cycles in CA_4.4). Same classification also applied to CA_4.2 and 4.6

with different boundaries with cycle number. In stage 1, the drift patterns of charge-discharge endpoints resembled (up to about 15 cycles in all three cells, as shown in the plots in **Fig. 4**), suggesting almost identical mechanistic in degradation, where Li inventory loss was negligible while slow Li diffusion and Li gradient buildup as hysteresis eroded the utilization efficiency. Stage 2 marked the accumulative Li inventory loss began to require Li supply from the anode, but the rate of inventory loss was quite different in each cell, i.e., CA_4.4 > CA_4.2 > CA_4.6, as inferred from the disparity in **Fig. 4j-l** and simultaneous declines in $\mathbf{U_{dis}}$ and $\mathbf{U_{ch}}$ (**Fig. 4g-i**). The sustainability of excess Li inventory from the anode shall determine the extent of lifespan in each case. A detailed comparison of **Fig. 4j-l** is shown in **Fig. 5**.

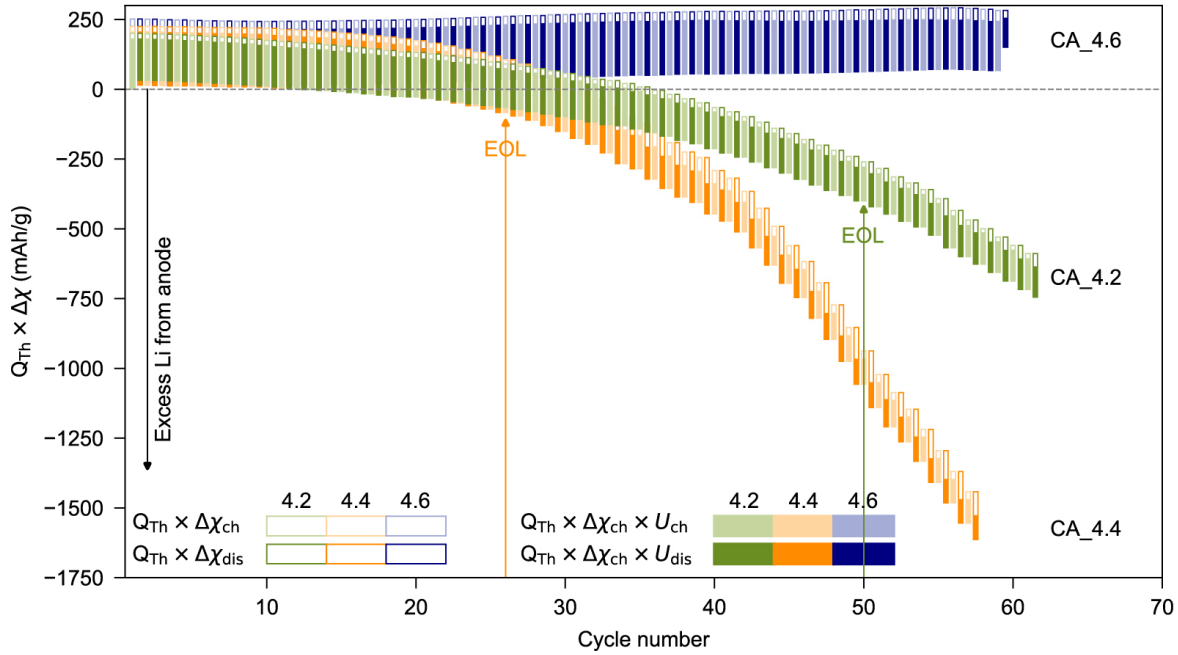

Fig. 5 | Trace of variations in ($Q_{Th} \times \Delta x$) as a function of cycle number. The traces indicate the reliance on excess Li from anode to sustain the capacity retention.

Here, a better perspective emerges: CA_4.2 reached the end-of-life (EOL) of 80% capacity retention in cycle 50, where excess Li inventory transactions from the anode shown by ($Q_{Th} \times \Delta x$) were in the –250 to –400 mAh g^{-1} range where $\mathbf{U_{dis}} \sim 0.75$, $\mathbf{U_{ch}} \sim 0.89$, and the ratio $\mathbf{U_{dis}}/\mathbf{U_{ch}} < 0.85$ were inferred at EOL. This scenario seems to represent a typical EOL condition where the loss of Li inventory was the determining factor in cycle life. In contrast, CA_4.4 reached EOL at cycle 26, while the Li inventory balance was still in stage 2, but $\mathbf{U_{ch}}$ (~0.85) and $\mathbf{U_{dis}}$ (~0.76) had declined noticeably, so did the $\mathbf{U_{dis}}/\mathbf{U_{ch}}$ ratio. A low $\mathbf{U_{dis}}$ seems to be the deciding factor for EOL, but not always. The Li anode in CA_4.6 performed better than the other two. Thus, in CA_4.6 the Li inventory balance sustained in stage 1 through the test. Interestingly, but not so surprised, the cyclability of Li anode was the determining factor in cell performance and life, which is hard to predict or determine the useful life for Li metal batteries. Therefore, the ability to track Li inventory as key indices in performance and degradation at the cell level provides more in-depth and relevant information to monitor and evaluate state of the battery—which is the center piece of this approach. To further validate the reliability of the Li inventory

analysis and tracking, **Supplementary Figs. 6** and **7** and details in **Supplementary Discussion** provide additional evidence using an analysis of a cycle-aged Cu | LHCE | NMC 811 cell. We demonstrate a consistent trend in capacity fade and loss of Li inventory but also the discrepancy between them as explained in **Supplementary Fig. 2**.

Conclusions

The benefit of Li inventory tracking was demonstrated in this work. Applying the principle of Gibbs free energy of formation which depicts a precise correspondence between equilibrium electrode potential V_{eq} and Li content x in NMC 811, we showed a reliable electrochemical analytic to convert experimental results into a thermodynamic framework based on V_{eq} vs. x correspondence for detailed quantitative analyses. The method projected stoichiometric changes in the region of the electrode near the cathode-electrolyte interface against the voltage measured at the current contact leads by a battery testing or power control device. The V_{eq} vs. x profile represents the Li concentration excursion induced by the charge-discharge process in the most sensitive and vulnerable region of the cathode. The analysis revealed the utilization of the cathode during polarization, deducing a utilization coefficient to relate the capacity and interfacial Li content change in a proper correspondence in the process. This approach offers a thermodynamic framework to trace Li inventory consistently and accurately as a cross-platform technique to compare cells with variations in cell formulations and test conditions. Insightful cell performance and degradation could be rationalized to understand the origin of the variations and their impact on performance.

This analytic Li inventory tracking approach demonstrates a possibility and capability of how electrochemical data analytics can accurately perform battery diagnosis and prognosis using a thermodynamic framework to achieve reliable and consistent analyses and rationalize battery performance and degradation. All the examples hereabove explicitly pointed to a discrete and tangible ability in this approach—the ability to track key indices of cell performance and degradation (x, **U**, and Li inventory), quantify uncertainties and clarify ambiguities in the experimental results that are difficult to decipher by empirical capacity analyses. This approach has potential to conduct a systematic failure tree analysis and failure modes and effects analysis to yield verifiable and quantitative relationships. This capability can be remarkably beneficial to battery research and manufacturing sectors to accelerate maturation of battery technology and lead to a reliable supply chain. More demonstrations on evaluation of cell performance, optimization by material engineering, electrode design, electrolyte formulation, cell balancing, and operating protocols; and precise battery state estimations could be anticipated, even though some challenges exist (More discussion on challenges is provided in **Supplementary Note 1**). We hope this capability could change the paradigm in battery engineering and development to accelerate its maturation.

Methods

Electrode Preparation

Targray NMC 811 powder was mixed with acetylene black (Alfa Aesar, 100% compressed, > 99.9%) and PVDF powder in a weight ratio of 90:5:5 in NMP solvent. The solid content is estimated to be ~45%. In the slurry preparation, the NMC 811 powder was mixed with acetylene black in a mixer (Thinky ARE 310) at 1,000 rpm for ~30 min first. Then, in stepwise, adding proper portions of PVDF/NMP solution with additional NMP at 2,000 rpm for another 30 min to produce desired slurry. To prepare cathode, the coatings were performed by the coating machine at Binghamton's Battery Facilities in a dry room. The slurry was coated on a 12 μm Al foil by the coating machine in a single-sided or double-sided format. The mass loading of a single-sided coating is ~17 mg cm^{-2}. The machine coated Targray NMC 811 cathode was dried already after coating through the two drying zones of the coating machine. The electrodes were then heat calendered to 3.0 g cm^{-3} and punched with a punch machine to the size of 84 mm L × 56 mm W for pouch cell fabrication.

EcoPro cathode composition is the same as Targray's. To prepare the slurry, PVDF was dissolved in NMP first, then in stepwise acetylene black and NMC 811 powder were added in small portions into the Thinky mixer at the speed of 2,000 rpm for ~20 min. The cathode was made by casting the formed homogeneous slurry onto an Al foil with doctor blade (~375 μm gap) to achieve a mass loading of the active material at around 17~18 mg cm^{-2}. The coated electrode was initially dried in air in an oven at 80°C for several hours before vacuuming dried for overnight. The dried electrodes were calendered to 3.0 g cm^{-3} and punched into proper discs with diameter of 12.7 mm for coin cell making.

All punched and calendered electrodes were further vacuum dried at 120°C for 2 h before transferring to a glovebox for coin cell assembling or pouch cell making in the dry room. Due to the high surface sensitivity of NMC 811 toward moisture, all the electrode preparations were operated in a dry room (with relative humidity < 0.5%). For the calendering density calculation, all solid materials on the Al current collector, including NMC 811, PVDF binder and carbon black, were counted.

Cell Making

The 2325-type coin cells were assembled for the electrochemical measurements with Li foil (250 μm) as a counter/reference electrode. Celgard 3501 separator was used. The electrolyte (Gotion LP30 electrolyte) comprised 1.0 M $LiPF_6$ dissolved in EC-DMC solution (1:1 in weight).

The pouch cells were made in the dry room with a double-side coated Targray NMC 811 cathode, each side facing a Li foil (100 μm thick) laminated on a 10 μm Cu current collector. A 20 μm polyethylene separator and Gotion LP30 electrolyte were used. More detail of the cell assembly is shown in **Supplementary Fig. 8**.

Electrochemical Measurements

For formation cycle, the pristine T or E cells were charged and discharged at C/10 (here Q = 200 mAh g^{-1} is typically used for coin cells) between 2.8 V and 4.4 V. Between the charge and

the discharge segments, a 15-min rest period was imposed to let voltage relax. At EOD, a constant voltage discharge step was held at 2.8 V for 24 hours or until the current reduced to C/100.

For GITT measurement, the pristine E-C cell was charged and discharged with C/20 for 1 hour followed by a six-hour rest to reach equilibrium at each intermittent state between V_{max} and V_{min} in each respective cell and test condition.

For cycle aging, charge-discharge cycles between 2.8 V and V_{max} = 4.2, 4.4, or 4.6 V at C/3 rate as specified for the corresponding cells were used.

Data Availability

All data used in this work are contained in the article and Supplementary Information. The datasets are also available at https://doi.org/10.17605/OSF.IO/2W4K3.

Acknowledgements

The work presented in this article comprised three stages of effort and development that should be recognized. The initial concept was developed in a project supported in part under Idaho National Laboratory's Laboratory Directed Research and Development program (Project No. 19P45-013FP) for a lithium-ion battery reliability and safety diagnostic study. This work was later supported by the project funded by the Assistant Secretary for Energy Efficiency and Renewable Energy, Office of Vehicle Technologies of the U.S. Department of Energy in the Advanced Battery Materials Research Program (Battery500 Consortium) to apply the concept to diagnose performance and degradation of high-energy rechargeable lithium metal batteries, where the bulk of the data was used in this study. The extension of the experimental work for the analysis is supported under Earth-Abundant Cathode Material Consortium led by Argonne National Laboratory and the goal is to assist material research with a better diagnostic tool and approach. Idaho National Laboratory is operated by Battelle Energy Alliance under Contract No. DE-AC07-05ID14517 for the U.S. Department of Energy.

Author Contributions

BL and ML conceived the conceptual approach for the analysis. ML and YZ conducted the analyses. HZ, FX, and MSW conducted the experiments and produced the data for the analyses. BL wrote the manuscript with the help of all authors.

Competing Interests

BL, ML, and YZ disclosed that Battelle Energy Alliance has filed U.S. Patent Applications: 17/149,046 and 18/185,018. U.S. Patent 11,740,290 has been issued. The remaining authors declare no competing interests.

References

1. Xiao, J. et al. Understanding and applying coulombic efficiency in lithium metal batteries. *Nat. Energy* **5**, 561–568 (2020). https://doi.org/10.1038/s41560-020-0648-z
2. Tornheim, A. & O'Hanlon D. C. What do Coulombic efficiency and capacity retention truly measure? A deep dive into cyclable lithium inventory, limitation type, and redox side reactions. *J. Electrochem. Soc*. **167**, 110520 (2020). DOI 10.1149/1945-7111/ab9ee8
3. Bond, T. M., Burns, J. C., Stevens, D. A., Dahn, H. M. & Dahn, J. R. Improving precision and accuracy in coulombic efficiency measurements of Li-ion batteries. *J. Electrochem. Soc*. **160**, A521–A527 (2013). http://dx.doi.org/10.1149/2.014304jes
4. Smith, A. J., Burns, J. C., Trussler, S. & Dahn, J. R. Precision measurements of the coulombic efficiency of lithium-ion batteries and of electrode materials for lithium-ion batteries. *J. Electrochem. Soc*. **157**, A196–A202 (2010). https://dx.doi.org/10.1149/1.3268129jes
5. Gyenes, B., Stevens, D. A., Chevrier, V. L. & Dahn, J. R. Understanding anomalous behavior in coulombic efficiency measurements on Li-ion batteries. *J. Electrochem. Soc*. **162**, A278–A283 (2015). http://dx.doi.org/10.1149/2.0191503jes
6. Adams, B. D., Zheng, J., Ren, X., Xu, W. & Zhang, J. G. Accurate determination of Coulombic efficiency for lithium metal anodes and lithium metal batteries. *Adv. Energy Mater*. **8**, 1702097 (2018). https://doi.org/10.1002/aenm.201702097
7. Li, X., Sun, X., Hu, X., Fan, F., Cai, S., Zheng, C. & Stucky, G. D. Review on comprehending and enhancing the initial Coulombic efficiency of anode materials in lithium-ion/sodium-ion batteries. *Nano Energy* 105143 (2020). https://doi.org/10.1016/j.nanoen.2020.105143
8. Li, Z., Huang, J., Liaw, B. Y. & Zhang, J. On state-of-charge determination for lithium-ion batteries. *J. Power Sources* **348**, 281–301 (2017). https://doi.org/10.1016/j.jpowsour.2017.03.001
9. Dubarry, M., Vuillaume, N. & Liaw, B. Y. Origins and accommodation of cell variations in Li-ion battery pack modeling. *Int. J. Energy Res*. **34**, 216–231 (2010). https://doi.org/10.1002/er.1668
10. Dubarry, M., Svoboda, V., Hwu, R. & Liaw, B. Y. Capacity loss in rechargeable lithium cells during cycle life testing: The importance of determining state-of-charge. *J. Power Sources* **174**, 1121–1125 (2007). http://dx.doi.org/10.1016/j.jpowsour.2007.06.185
11. Dubarry, M., Truchot, C., Cugnet, M., Liaw, B. Y., Gering, K., Sazhin, S., Jamison, D. & Michelbacher, C. Evaluation of commercial lithium-ion cells based on composite positive electrode for plug-in hybrid electric vehicle applications. Part I: Initial characterizations. *J. Power Sources* **196**, 10328–10335 (2011). https://doi.org/10.1016/j.jpowsour.2011.08.077
12. Wang, F., Lin, Z., Liu, L., Wei, X., Lin, S., Dai, L., Wei, Y., Liaw, B. & Liang, C. Does polarization increase lead to capacity fade? *J. Electrochem. Soc*. **167**, 090549 (2020). https://doi.org/10.1149/1945-7111/ab956b

13. Zhang, Y., Wang, Q., Liaw, B., Nagpure, S. C., Dufek, E. J. & Dickerson, C. C. A quantitative failure analysis on capacity fade in rechargeable lithium metal cells. *J. Electrochem. Soc*. **167**, 090502 (2020). https://doi.org/10.1149/1945-7111/ab6cf4
14. Zhang, Y., Wang, Q., Liaw, B., Nagpure, S. C., Dufek, E. J. & Dickerson, C.C. Cell qualification—A performance metric-based approach. *J. Phys. Energy* **2**, 034003 (2020). https://doi.org/10.1088/2515-7655/ab979b
15. Liu, J., Bao, Z., Cui, Y. *et al.* Pathways for practical high-energy long-cycling lithium metal batteries. *Nat. Energy* **4**, 180–186 (2019). https://doi.org/10.1038/s41560-019-0338-x
16. Kasnatscheew, J., Evertz, M., Streipert, B., Wagner, R., Klopsch, R. K., Vortmann, B., Hahn, H., Nowak, S., Amereller, M., Gentschev, A.-C., Lamp, P. & Winter, M. The truth about the 1st cycle Coulombic efficiency of $LiNi_{1/3}Co_{1/3}Mn_{1/3}O_2$ (NCM) cathodes. *Phys. Chem. Chem. Phys*. **18**, 3956–3965 (2016). https://doi.org/10.1039/C5CP07718D
17. Kang, S.-H., Yoon, W.-S., Nam, K.-W., Yang, X.-Q. & Abraham, D. P. Investigating the first-cycle irreversibility of lithium metal oxide cathodes for Li batteries. *J. Mater. Sci*. **43**, 4701–4706 (2008). https://doi.org/10.1007/s10853-007-2355-6
18. Choi, J. & Manthiram, A. Investigation of the irreversible capacity loss in the layered $LiNi_{1/3}Co_{1/3}Mn_{1/3}O_2$ cathodes. *Electrochem. Solid-State Lett*. **8**, C102–C105 (2005). https://doi.org/10.1149/1.1943567
19. Zhang, S. S., Xu, K. & Jow, T. R. Formation of solid electrolyte interface in lithium nickel mixed oxide electrodes during the first cycling. *Electrochem. Solid-State Lett*. **5**, A92–A94 (2002). https://doi.org/10.1149/1.1464506
20. Lee, K.-K. & Kim, K.-B. Electrochemical and structural characterization of $LiNi_{1-2y}Co_yO_2$ ($0 \leq y \leq 0.2$) positive electrodes during initial cycling. *J. Electrochem. Soc*. **147**, 1709–1717 (2000). https://doi.org/10.1149/1.1393422
21. Arai, H., Okada, S., Sakurai, Y. & Yamaki, J.-i. Reversibility of $LiNiO_2$ cathode. *Solid State Ionics* **95**, 275–282 (1997). https://doi.org/10.1016/S0167-2738(96)00598-X
22. Xin, F., Zhou, H., Chen, X., Zuba, M., Chernova, N., Zhou, G. & Whittingham, M. S. Li–Nb–O coating/substitution enhances the electrochemical performance of the $LiNi_{0.8}Mn_{0.1}Co_{0.1}O_2$ (NMC 811) cathode. *ACS Applied Materials & Interfaces* **11**, 34889–34894 (2019). https://doi.org/10.1021/acsami.9b09696
23. Zhou, H., Xin, F., Pei, B. & Whittingham, M. S. What limits the capacity of layered oxide cathodes in lithium batteries? *ACS Energy Letters* **4**, 1902–1906 (2019). https://doi.org/10.1021/acsenergylett.9b01236
24. Märker, K., Reeves, P. J., Xu, C., Griffith, K. J. & Grey, C. P. Evolution of structure and lithium dynamics in $LiNi_{0.8}Mn_{0.1}Co_{0.1}O_2$ (NMC 811) cathodes during electrochemical cycling. *Chem. Mater*. **31**, 2545–2554 (2019). https://doi.org/10.1021/acs.chemmater.9b00140
25. Weppner W. & Huggins, R. A. Determination of the kinetic parameters of mixed-conducting electrodes and application to the system Li_3Sb. *J. Electrochem. Soc*. **124**, 1569–1578 (1977). https://doi.org/10.1149/1.2133112
26. Huggins, R. A. *Advanced Batteries: Materials Science Aspects*. Springer (2008). DOI: 10.1007/978-0-387-76424-5

27. Li, Z. Yin, L., Mattei, G. S., Cosby, M. R., Lee, B.-S., Wu, Z., Bak, S.-M., Chapman, K. W., Yang, X.-Q., Liu, P. & Khalifah, P. G. Synchrotron operando depth profiling studies of state-of-charge gradients in thick $Li(Ni_{0.8}Mn_{0.1}Co_{0.1})O_2$ cathode films. *Chem. Mater*. **32**, 6358−6364 (2020). https://dx.doi.org/10.1021/acs.chemmater.0c00983?ref=pdf
28. Mao, Y., Wang, X., Xia, S., Zhang, K., Wei, C., Bak, S., Shadike, Z., Liu, X., Yang, Y., Xu, R., Pianetta, P., Ermon, S., Stavitski, E., Zhao, K., Xu, Z., Lin, F., Yang, X.-Q., Hu, E. & Liu, Y. High-voltage charging-induced strain, heterogeneity, and micro-cracks in secondary particles of a nickel-rich layered cathode material. *Adv. Funct. Mater*. **29**, 1900247 (2019). https://doi.org/10.1002/adfm.201900247
29. Wu, F., Dong, J., Chen, L., Chen, G., Shi, Q., Nie, Y., Lu, Y., Bao, L., Li, N., Song, T., et al. Removing the intrinsic NiO phase and residual lithium for high-performance nickel-rich materials. *Energy Mater. Adv*. **4**, 0007 (2023). https://doi.org/10.34133/energymatadv.0007
30. Rahimi Eichi H. & Chow, M.-Y. Modeling and analysis of battery hysteresis effects. Proc. of 2012 IEEE Energy Conversion Congress and Exposition (ECCE 2012), pp. 4479-4486 (2012). https://doi.org/10.1109/ECCE.2012.6342212.
31. Lim, J. et al. Origin and hysteresis of lithium compositional spatiodynamics within battery primary particles. *Science* **353**, 566–571 (2016). https://doi.org/10.1126/science.aaf4914
32. Hess, M., Sasaki, T., Villevieille, C. & Novák, P. Combined operando X-ray diffraction-electrochemical impedance spectroscopy detecting solid solution reactions of $LiFePO_4$ in batteries. *Nat. Commun*. **6**, 8169 (2015). https://doi.org/10.1038/ncomms9169
33. Ovejas, V.J., Cuadras, A. Effects of cycling on lithium-ion battery hysteresis and overvoltage. *Sci. Rep.* **9**, 14875 (2019). https://doi.org/10.1038/s41598-019-51474-5
34. Fang, Z., Confer, M., Wang, Y., Wang, Q., Kunz, M. R., Dufek, E. J., Liaw, B., Klein, T., Dixon, D. & Fushimi, R. Formation of surface impurities on lithium-nickel-manganese-cobalt oxides in the presence of CO_2 and H_2O. *J. Am. Chem. Soc.* **143**, 10261–10274 (2021). https://doi.org/10.1021/jacs.1c03812
35. Gering, K. L., Sazhin, S. V., Jamison, D. K., Michelbacher, C. J., Liaw, B. Y., Dubarry, M. & Cugnet, M. Investigation of path dependence in commercial lithium-ion cells chosen for plug-in hybrid vehicle duty cycle protocols. *J. Power Sources* **196**, 3395–3403 (2011). https://doi.org/10.1016/j.jpowsour.2010.05.058
36. Su, L., Zhang, J., Huang, J., Ge, H., Li, Z., Xie, F. & Liaw, B. Y. Path dependence of lithium ion cells aging under storage conditions. *J. Power Sources* **315**, 35–46 (2016). https://doi.org/10.1016/j.jpowsour.2016.03.043